INTERNATIONAL JOURNAL FOR NUMERICAL METHODS IN FLUIDS
Int. J. Numer. Meth. Fluids 2006; **52**:883–902
Published online 16 March 2006 in Wiley InterScience (www.interscience.wiley.com). DOI: 10.1002/fld.1208

Unsteady RANS simulation of oscillating mould flows

R. Schwarze*,†

Institut für Mechanik und Fluiddynamik, Technische Universität Bergakademie Freiberg, Lampadiusstr. 4, 09596 Freiberg, Germany

SUMMARY

Mould flow oscillations are of major importance for the performance of the continuous casting process. They are suspected to promote entrainment of slag and other unwanted secondary phases into the melt pool. These oscillating turbulent flows are investigated by means of numerical simulations. The numerical model is based on the equation of continuity and the unsteady Reynolds averaged Navier–Stokes equations. The system of flow equations is closed by a Reynolds stress turbulence model in combination with non-equilibrium wall functions.

The unsteady simulation resolves low-frequency oscillations of the flow field. These frequencies and numerically resolved mean values are in agreement with results of corresponding model experiments.

The proposed model should be advantageous in order to investigate the mechanisms of the oscillations and the process of slag entrainment in more detail. Copyright © 2006 John Wiley & Sons, Ltd.

KEY WORDS: continuous casting mould; unsteady RANS; oscillating flow; vortex shedding

1. INTRODUCTION

Detailed knowledge of flow features in continuous casting moulds is highly desirable because this flow region is of major importance for the quality of the final strand. Industrial-scale experiments are almost impossible due to the physical and chemical properties of the melt. Hence, an improved understanding of the heat and fluid flow processes in these facilities requires mainly numerical modelling [1]. Numerical simulations combined with laboratory-scale isothermal model experiments have been applied successfully in order to resolve the main features of mould flows, see, e.g. Reference [2] for a review.

Figure 1(a) displays a common mould configuration. The melt pool is continuously fed through the ports of the submerged entry nozzle (SEN) while the solidifying steel is driven

*Correspondence to: R. Schwarze, Institut für Mechanik und Fluiddynamik, Technische Universität Bergakademie Freiberg, Lampadiusstr. 4, 09596 Freiberg, Germany.
†E-mail: Ruediger.Schwarze@imfd.tu-freiberg.de

Received 28 July 2005
Revised 25 January 2006
Accepted 25 January 2006

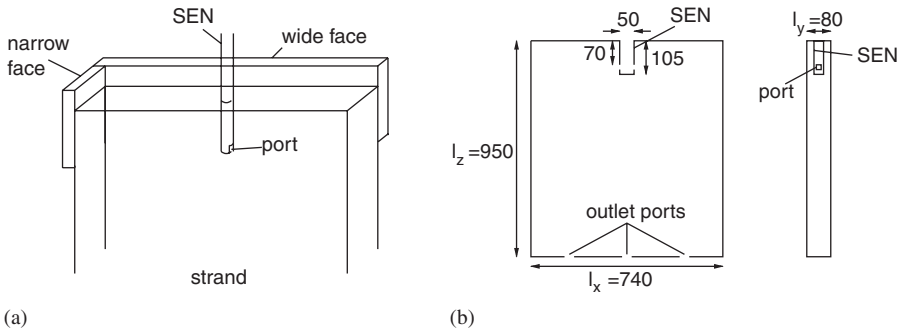

Figure 1. Typical mould geometry and details of the investigated configuration: (a) geometry; and (b) model configuration.

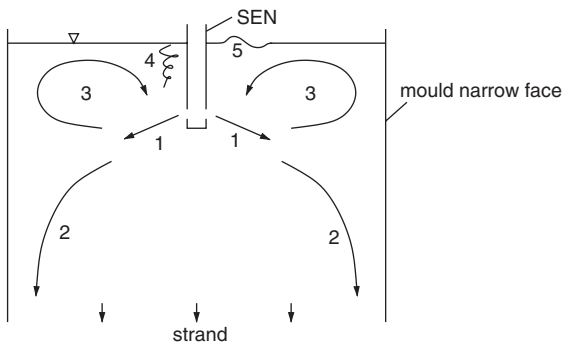

Figure 2. Main features of mould flows.

downwards to the strand. The pool is bounded by opposed pairs of the narrow and the wide face of the mould.

Figure 1(b) shows the mould geometry, which is investigated in the present paper. The sizes correspond to the 0.4-scale water model experiment of Yuan *et al.* [3]. The flow enters the mould through two ports of the cylindrical SEN and leaves through three outlet ports. The lengths of the mould are given in mm. The size of a SEN port is $30 \times 30\,\mathrm{mm}^2$ whereas the size of an outlet port is $23 \times 80\,\mathrm{mm}^2$.

Prominent features of the mould flow field are sketched in Figure 2. Jet flows (1) develop immediately downstream of the SEN ports. These jets are splitted and deflected by the mould narrow faces. Secondary jet streams (2) are directed downwards to the lower bulk of the mould. The Reynolds numbers of the jet flows (1) are $Re_\mathrm{j} \sim 12\,000$, based on the hydrodynamic diameter $d_\mathrm{p} = 30\,\mathrm{mm}$ of the SEN ports and the maximum velocity $u_j = 0.45\,\mathrm{m/s}$ in the jet. The Reynolds number of the bulk flow in the mould is $Re_\mathrm{b} \sim 3000$, based on the hydrodynamic diameter $d_\mathrm{m} = 150\,\mathrm{mm}$ of the mould and the mean velocity $u_m = 0.02\,\mathrm{m/s}$ of the mould flow. Other secondary jet streams are driven upwards and form rotating eddies (3). These eddies stimulate funnel-shaped vortices (4) and waves (5) at the top surface of the

melt pool. Actually, these transient surface processes are of great interest. They are suspected to promote steel quality problems due to slag and bubble entrainment into the melt [4].

Recently, some efforts have been made in order to resolve the unsteady behaviour of mould flows in more detail. Gupta *et al.* [5] observed in a water model study, that the mould flow patterns are oscillating. Other authors investigated transient mould flow features by means of numerical simulations, e.g. in References [3, 4, 6].

Huang *et al.* [4] investigate transitions from uneven to even mould flows numerically. Here, uneven flow means that the flow rates through the left and the right port of the SEN are different, whereas they are of the same intensity in case of even flow. The transient model is based on the Reynolds averaged flow equations. The k–ε turbulence model of Launder and Spalding [7] is employed in order to close the model equations. The simulation is started with initial values provided by steady uneven flow but with even flow boundary conditions. The solution domain contains 3×10^4 grid cells, the time step width is $\Delta t = 6.67$ s and computation time is 40 h on an IBM RS 6000 for 200 s of flow time. The authors find that the initially oscillating behaviour of the flow field is damped after $\tau = 200$ s flow time. They expect that these oscillations will be stronger in the steel caster and that the numerical results are strongly influenced by numerical viscosity, i.e. truncation errors due to the approximations in the numerical model.

Yuan *et al.* [3] compare results of a large-eddy simulation (LES) with experimental data from PIV measurements at the water model experiment sketched in Figure 1. The specifications of the LES model are 1.5×10^6 grid cells, subgrid-scale k model and time step width $\Delta t = 0.3$ ms. Computation time is 24 h on a Pentium IV 3.2 GHz PC for 1 s of flow time. The authors find a good agreement between the time-averaged flow fields of the experiment and of the simulation. However, transient flow data in selected points near the free top surface of the mould reveal some marked discrepancies. Instantaneous velocity data from the experiment expose different frequency regimes in the flow, high frequencies due to turbulent fluctuations and some distinct low frequencies due to long-term oscillations of the mould flow. On the contrary, LES data resolve only high frequencies of the turbulent flow. The LES, which covered a time interval of 51 s of flow time, cannot represent the long-term oscillating behaviour adequately.

Ramos-Banderas *et al.* [6] compare results of a LES with experimental data from a water model study, too. Unfortunately, numerical parameters of the LES are not given in the paper. The authors find acceptable qualitative agreement between experimental and numerical resolved flow structures. However, there are also some marked differences, e.g. about the transient behaviour of the rotating eddies (feature (3) in Figure 2). The authors conclude, that the capacities of the LES to resolve unsteady instantaneous flow fields in moulds are only limited.

Clearly, LES is the best method in order to investigate details of the turbulence of mould flows. However, an efficient and realizable numerical simulation of long-term oscillating mould flows is still an open goal. Therefore, a new numerical model of transient mould flows is presented in the paper. It is based on unsteady Reynolds averaged flow equations in combination with a Reynolds stress turbulence model. This approach is commonly termed URANS model. A more detailed discussion of URANS simulations is given, e.g. in References [8, 9].

URANS models have been successfully applied to other flow configurations, which are closely connected to mould flows: (i) unsteady flows in an induction furnace crucible [10], (ii) jet into a cavity and (iii) unsteady separated flow past a cylinder. Mataoui *et al.* [11]

investigate interactions between a plane turbulent jet into a rectangular cavity. Here, the Reynolds number of the jet flow is $Re = 4000$. The authors compare the results of a URANS simulation to corresponding measurements at a wind tunnel experiment. They find different flow regimes (stable, unstable oscillations and stable oscillations), which depend on the location of the jet entrance in the cavity. The flow regimes are found in the experiment and in the numerical simulation as well.

Predictions of unsteady separated flows past cylinders are basic tests of URANS models. Among others, Iaccarino *et al.* [9], Catalano *et al.* [12] and Johansen *et al.* [13] have successfully performed such URANS simulations. Predicted Strouhal numbers of the shedding cycle in the cylinder wake are in accordance with corresponding experimental measurements.

In this paper, an URANS model is employed in order to investigate long-term oscillations of mould flows. The transient results of the simulation runs are inspected and analysed in detail. Qualitative and quantitative features of the oscillating flows will be compared with experimental findings from the isothermal water model study reported by Yuan *et al.* [3].

2. NUMERICAL MODEL

2.1. URANS equations

The mould flow is considered as incompressible and isothermal, hence the fluid motion is described by the equation of continuity and the Navier–Stokes equations

$$\frac{\partial u_i}{\partial x_i} = 0 \tag{1}$$

$$\frac{\partial u_i}{\partial t} + \frac{\partial}{\partial x_j}(u_j u_i) = -\frac{1}{\rho}\frac{\partial p}{\partial x_i} + \frac{\partial}{\partial x_j}\left(\nu \frac{\partial u_i}{\partial x_j}\right) \tag{2}$$

Here, u_i is the velocity and p is the pressure. The material parameters are density $\rho = 1000\,\mathrm{kg/m^3}$ and kinematic viscosity $\nu = 10^{-6}\,\mathrm{m^2/s}$. The mould flow contains large coherent structures, whose oscillations should be resolved. Therefore, the URANS model is based on a triple decomposition of the flow quantities ϕ

$$\phi(t) = \overline{\phi} + \tilde{\phi}(t) + \phi'(t) \tag{3}$$

where $\overline{\phi}$ is the mean of a flow quantity, $\tilde{\phi}$ and ϕ' indicate resolved oscillations and turbulent fluctuations, respectively. It is assumed, that the time scale τ_{osc} of $\tilde{\phi}$ is significantly larger than the characteristic turbulent time scale τ_{turb} and that time-filtered quantities are determined by

$$\langle \phi \rangle = \overline{\phi} + \tilde{\phi}(t) = \frac{1}{\tau}\int_{t_0}^{t_0+\tau} \phi \, \mathrm{d}t \tag{4}$$

with $\tau_{\mathrm{turb}} \ll \tau \ll \tau_{\mathrm{osc}}$. Finally, the mean quantity results from a long-term average of ϕ

$$\overline{\phi} = \lim_{t_\infty \to \infty} \frac{1}{t_\infty}\int_{t_0}^{t_0+t_\infty} \phi \, \mathrm{d}t \tag{5}$$

The time-filtered equation of continuity and the time-filtered Navier–Stokes equations are

$$\frac{\partial\langle u_i\rangle}{\partial x_i}=0 \tag{6}$$

$$\frac{\partial\langle u_i\rangle}{\partial t}+\frac{\partial}{\partial x_j}(\langle u_j u_i\rangle)=-\frac{1}{\rho}\frac{\partial\langle p\rangle}{\partial x_i}+\frac{\partial}{\partial x_j}\left(\nu\frac{\partial\langle u_i\rangle}{\partial x_j}\right) \tag{7}$$

With the turbulent stress tensor

$$\tau_{ij}=(\langle u_j\rangle\langle u_i\rangle-\langle u_j u_i\rangle) \tag{8}$$

the unknown time-filtered velocity products $\langle u_j u_i\rangle$ in Equation (7) are replaced by the product of the resolved time-filtered velocities $\langle u_j\rangle\langle u_i\rangle$:

$$\frac{\partial\langle u_i\rangle}{\partial t}+\frac{\partial}{\partial x_j}(\langle u_j\rangle\langle u_i\rangle)=-\frac{1}{\rho}\frac{\partial\langle p\rangle}{\partial x_i}+\frac{\partial}{\partial x_j}\left(\nu\frac{\partial\langle u_i\rangle}{\partial x_j}+\tau_{ij}\right) \tag{9}$$

Equations (6) and (9) give the resolved flow field, where the velocity $\langle u_i\rangle$ and the pressure $\langle p\rangle$ are assumed to be implicitly time-filtered. The turbulent stress tensor τ_{ij} in Equation (9) gives the contributions of the unresolved turbulent fluctuations on the resolved flow. The individual stresses must be provided by a suitable turbulence model. For this purpose, the Reynolds stress model in the basic formulation of Launder *et al.* [14] is employed. Here, the turbulent stresses are given by

$$\frac{\partial\tau_{ij}}{\partial t}+\langle u_l\rangle\frac{\partial\tau_{ij}}{\partial x_l}=D_{ij}^{\mathrm{mod}}+D_{ij}+P_{ij}+R_{ij}^{\mathrm{mod}}+\varepsilon_{ij}^{\mathrm{mod}} \tag{10}$$

The following terms of Equation (7) are in the closed form:

1. production

$$P_{ij}=-\tau_{il}\frac{\partial\langle u_j\rangle}{\partial x_l}-\tau_{jl}\frac{\partial\langle u_i\rangle}{\partial x_l} \tag{11}$$

2. molecular dissipation

$$D_{ij}=\nu\frac{\partial^2\tau_{ij}}{\partial x_l^2} \tag{12}$$

The remaining terms have to be approximated. The turbulent diffusion D_{ij}^{mod} is modelled due to a scalar gradient approach [15]:

$$\begin{aligned} D_{ij}^{\mathrm{mod}}&=\frac{\partial}{\partial x_l}\left(\langle u_i' u_j' u_l'\rangle+\left\langle\frac{p'}{\rho}u_i'\delta_{lj}\right\rangle+\left\langle\frac{p'}{\rho}u_j'\delta_{li}\right\rangle\right)\\ D_{ij}^{\mathrm{mod}}&=\frac{\partial}{\partial x_l}\left[\frac{\nu_t}{\sigma_k}\frac{\partial\tau_{ij}}{\partial x_l}\right] \end{aligned} \tag{13}$$

The pressure strain term R_{ij}^{mod} is modelled due to the proposal of Launder *et al.* [14]

$$\begin{aligned} R_{ij}^{\mathrm{mod}} &= \left\langle \frac{p'}{\rho}\left(\frac{\partial u_i'}{\partial x_j}+\frac{\partial u_j'}{\partial x_i}\right)\right\rangle \\ R_{ij}^{\mathrm{mod}} &= c_1\frac{\varepsilon}{k}\left[\frac{2}{3}\rho k\,\delta_{ij}-\tau_{ij}\right]+c_2\left[\frac{2}{3}(P-C)\delta_{ij}-(P_{ij}-C_{ij})\right] \end{aligned} \tag{14}$$

Regarding the modelling of the dissipation, it is assumed, that the Reynolds numbers of the flow are sufficiently high in order to guarantee that Kolmogorovs assumption of local isotropy of the smallest scales is fulfilled where dissipation overwhelmingly occurs. Then, the dissipation rate $\varepsilon_{ij}^{\mathrm{mod}}$ can be modelled by

$$\begin{aligned} \varepsilon_{ij}^{\mathrm{mod}} &= \nu\left\langle \frac{\partial u_i'}{\partial x_k}\frac{\partial u_j'}{\partial x_k}\right\rangle \\ \varepsilon_{ij}^{\mathrm{mod}} &= \tfrac{2}{3}\varepsilon\,\delta_{ij} \end{aligned} \tag{15}$$

Finally, the quantities ν_t, ε, k, P and C in Equations (13)–(15) are modelled like in k–ε models, i.e.

$$\nu_t = c_\mu\frac{k^2}{\varepsilon} \tag{16}$$

$$\frac{\partial\varepsilon}{\partial t}+\langle u_j\rangle\frac{\partial\varepsilon}{\partial x_j}=\frac{\partial}{\partial x_l}\left[\left(\nu+\frac{\nu_t}{\sigma_\varepsilon}\right)\frac{\partial\varepsilon}{\partial x_l}\right]+c_{\varepsilon1}P\frac{\varepsilon}{k}-c_{\varepsilon2}\frac{\varepsilon^2}{k} \tag{17}$$

$$k=\frac{\langle u_l'u_l'\rangle}{2}=-\frac{\tau_{ll}}{2\rho} \tag{18}$$

$$P=\frac{P_{ll}}{2} \tag{19}$$

$$C=\frac{C_{ll}}{2} \tag{20}$$

The coefficients in the Reynolds stress model are fixed to $\sigma_k=0.82$, $c_1=1.8$, $c_2=0.6$, $c_\mu=0.09$, $\sigma_\varepsilon=1.0$, $c_{\varepsilon1}=1.44$, $c_{\varepsilon2}=1.92$. These coefficients have been recommended by Gibson and Launder [16].

2.2. Boundary conditions and initial values

The boundary conditions imposed for the numerical simulations are as follows:

- The velocity in the SEN ports is $u_{\mathrm{SEN}}=0.45\,\mathrm{m/s}$. This fits to the corresponding flow rate $\dot{V}=0.71\,\mathrm{l/s}$ in the experiment conducted by Yuan *et al.* [3]. The velocity is directed downwards at a fixed angle of 30° with respect to the top mould surface. This value is deduced from the time-averaged PIV data in Reference [3] as the emphasis of the present paper is placed on the flow behaviour within the mould. Boundary conditions for the turbulence in the inlet are estimated from the supposed turbulence intensity $\mathrm{ti}=0.1$ and the hydrodynamic diameter $d_{\mathrm{p}}=30\,\mathrm{mm}$ of the SEN ports.

- A pressure boundary condition $p_{\mathrm{OUT}} = 10^5$ Pa (ambient pressure) is imposed at the outlet ports.
- The top surface of the mould remains flat. A no-shear condition is applied here. This condition should model the behaviour of the free surface in the water model experiment.
- No-slip conditions at all rigid walls. The velocity and the turbulence quantities close to the wall are determined according to non-equilibrium wall functions [17], see below.

The basic ideas of the non-equilibrium wall function approach are as follows:

1. The ordinary wall functions are sensitized to pressure-gradient effects. Therefore, the functional relationship of the log-of-the-wall law is enhanced from $u^+ = f(y^+)$ to $u^+ = f(y^+, p^+)$. Here, y^+ is the non-dimensional wall normal distance, whereas u^+ and p^+ are the non-dimensional velocity and the non-dimensional pressure gradient tangential to the wall, respectively.
2. Commonly, turbulence production and dissipation are assumed to be in equilibrium in the wall-neighbouring cells. With the framework of the non-equilibrium wall function, this condition is relaxed and turbulence production is allowed to deviate from dissipation.

The concept of non-equilibrium wall functions should result in a better description of near-wall flows with separation, reattachment, and impingement, which have to be dealt with in the present study.

The results of steady RANS simulations of the problem with corresponding boundary conditions provide initial values for the URANS simulation.

2.3. *Numerical details*

Equations (6), (9), (10) and (17) are solved by the finite-volume method. The commercial code FLUENT version 6.1 is employed for this purpose. The lower bound of the period τ of the time filter can be estimated from the turbulence quantities k and ε, as explained, e.g. in Johansen *et al.* [13]. The mean values in the mould flow determined by the ordinary RANS approach are $k_m = 0.604 \times 10^{-3}\,\mathrm{m^2/s^2}$ and $\varepsilon_m = 1.03 \times 10^{-3}\,\mathrm{m^2/s^3}$. Then, the characteristic turbulent time scale τ_{turb} can be estimated as

$$\tau_{\mathrm{turb}} = \frac{k_m}{\varepsilon_m} \simeq 0.6\,\mathrm{s} \tag{21}$$

Consequently, the temporal filtering, Equation (4), is implicitly included in Equations (6), (9), (10) and (17) as long as the period τ of the time filter is larger than the turbulent time scale τ_{turb}, i.e. $\tau \gg \tau_{\mathrm{turb}}$.

Time and space discretization schemes are implicit three-level time discretization, QUICK [18] upwind interpolation and central differencing for derivatives. Pressure interpolation on the non-staggered grid is performed due to Rhie and Chow's method [19]. The SIMPLE algorithm [20] is used for the iterative solution of all equations.

The iteration process for the initial RANS solution has been stopped, when the residuals of all quantities are lower than 0.002. In the unsteady simulations, 20 iterations are performed at each time step. Commonly, the residuals of all quantities are close to 0.001 after these 20 iterations.

Figure 3(a) gives the solution domain which has to be meshed. The dimensions of the domain are given in Figure 1(b). The numerical grids consist of hexahedral cells.

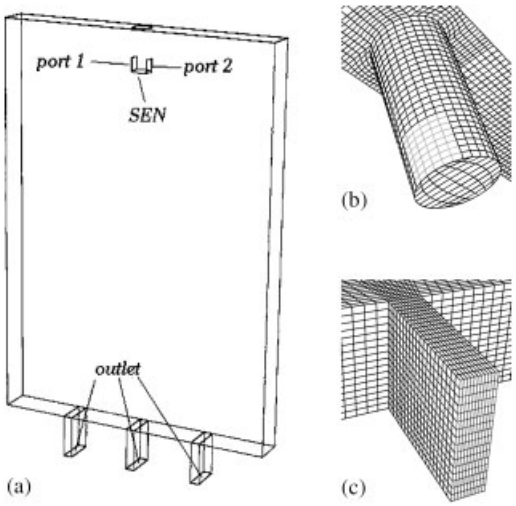

Figure 3. Grid details: (a) mould geometry; (b) SEN; and (c) outlet.

Table I. Specifications of simulations.

Grid	Δt_1	Δt_2	Δt_3
Coarse	$C1$	$C2$	$C3$
Fine	—	—	F

Attention has been paid in order to guarantee that the cells are almost equilateral and rectangular. Only grid regions near the SEN (Figure 3(b)) and towards the outlet (Figure 3(c)) do not meet these conditions. The regular mesh should help to minimize discretization errors.

The resolution of the boundary layer at the wide face determines the meshing process. Here, two opposed requirements have to be fulfilled: (i) The first grid point has to be placed outside the viscous sublayer. Commonly, $y^+ \geqslant 20$ is assumed as a suitable limit. (ii) The remaining part of the boundary layer has to be resolved at least with 8–10 grid points [21].

Two different numerical grids have been used in the simulations: The coarse grid consists of about 300 000 cells. The average spacing of the wall-nearest grid point to the wall is $y^+ = 17$. The fine grid consists of about 570 000 cells. Here, the average spacing of the wall-nearest grid point to the wall is $y^+ = 15$. Significantly finer or coarser grids would not resolve the boundary layer adequately, when wall functions are employed. Either requirement (i) or (ii) would be strongly violated. On the contrary, a complete resolution of the viscous sublayer would increase numerical efforts drastically.

All simulations cover $\tau_{\text{sim}} = 500\,\text{s}$ of flow time. They are performed with three different time step widths $\Delta t_1 = 0.025\,\text{s}$, $\Delta t_2 = 0.05\,\text{s}$ and $\Delta t_3 = 0.1\,\text{s}$. The specifications of the different simulations are explained in Table I. Computing 1 s of flow time requires approximately 40 min on a Pentium IV 3.0 GHz PC for the coarse grid and the time step width Δt_3.

3. RESULTS

3.1. Steady flow

Figures 4 displays features of the steady velocity field which has been calculated on the coarse grid. The basic structure of the flow is visualized by velocity vector plots in the vertical centreplane ($y = 0\,\text{mm}$) and near to the mould wide face ($y = 33\,\text{mm}$). The jet streams which develop downstream of the inlet ports drive two rotating eddies in the upper and two more eddies in the lower part of the model. The whole flow field is nearly symmetrical with respect to the mould lateral centreplane, but small deviations from symmetry are evident. These deviations are found in the RANS simulations on the coarse and on the fine grid.

Obviously, the numerical model does not reach the symmetrical solution exactly. This problem seems to be due to the fact, that the mould flow is inherently unsteady [22]. In a RANS simulation, each iteration can be interpreted as a small pseudo-time step, hence the residuals oscillate indefinitely around the unstable symmetric solution.

The magnitude and the direction of the flow velocity can be deduced from the velocity vectors in Figure 4. Longest vectors correspond to the inlet velocity $u_{\text{SEN}} = 0.45\,\text{m/s}$. It is found that the velocity in the upper eddies is substantially higher than in the lower ones.

3.2. Comparison of URANS results with experimental data

The oscillating mould flow is analysed in detail at several locations in the mould. Figure 5 indicates two points and two horizontal lines in the longitudinal centreplane, where time series of the velocity are recorded throughout the numerical simulations.

The results are compared with the findings of Yuan *et al.* [3]. They give profiles of mean velocity data measured in water model experiments. They also deduce oscillation periods from these experiments and a corresponding LES simulation.

Mean values of the horizontal velocity $\overline{u}$ and the vertical velocity $\overline{w}$ are determined from a long-term average, Equation (4). Figure 6 shows numerically and experimentally

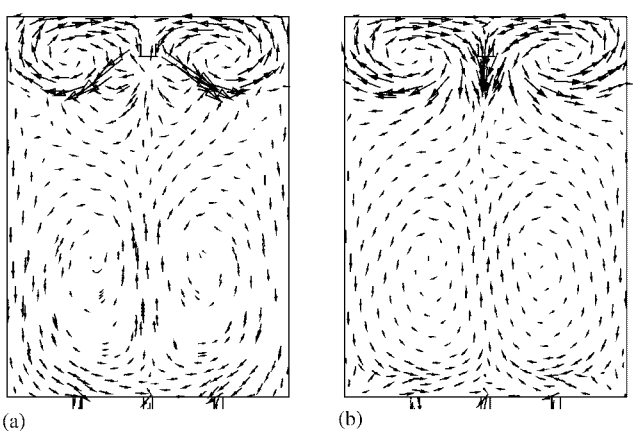

Figure 4. Velocity vectors in the steady flow field. Longest vectors correspond to the inlet velocity $u_{\text{SEN}} = 0.45\,\text{m/s}$. (a) $y = 0\,\text{mm}$ corresponds to the vertical centreplane of the mould; and (b) $y = 33\,\text{mm}$ is near to the mould wide face.

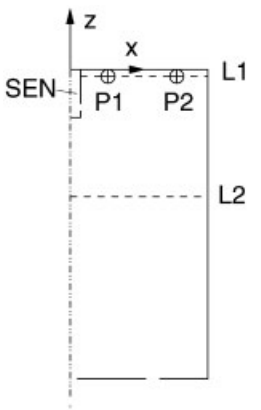

	x [m]	y [m]	z [m]
P1	0.10	0.0	-0.0015
P2	0.22	0.0	-0.0015
L1	—	0.0	-0.0015
L2	—	0.0	-0.40

Figure 5. Points and lines for detailed inspection.

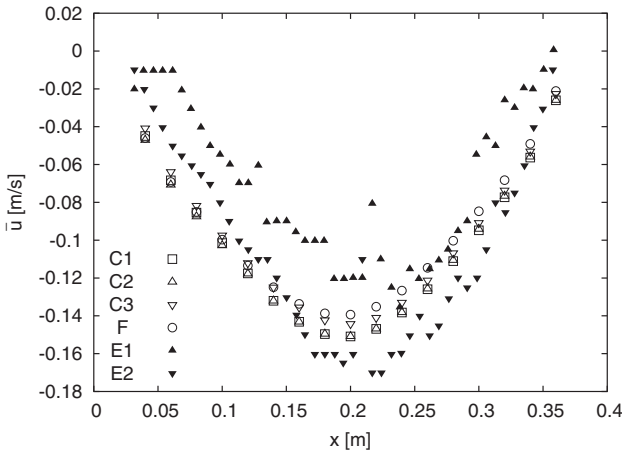

Figure 6. Mean horizontal velocity $\overline{u}$ along $L1$, results are from numerical simulations ($C1$, $C2$, $C3$, F) and PIV measurements ($E1$, $E2$).

determined profiles of the horizontal velocity $\overline{u}(x)$ along line $L1$. Experimental data stem from PIV measurements [3] at different flow rates $\dot{V}_1 = 0.65\,\mathrm{l/s}$ (denoted as $E1$) with a velocity $u_{\mathrm{SEN},E1} = 0.41\,\mathrm{m/s}$ in the SEN ports and $\dot{V}_2 = 0.92\,\mathrm{l/s}$ (denoted as $E2$) with $u_{\mathrm{SEN},E2} = 0.58\,\mathrm{m/s}$. Both experimental data sets reveal a bump between $x = 0.2$ and $0.25\,\mathrm{m}$. These features are not discussed in Reference [3]. May be systematic errors are made: PIV data were recorded only for 10 s. Hence, average values of PIV data still include some contributions of long-term fluctuating components.

Numerical data are deduced from the URANS simulations $C1$, $C2$, $C3$ and F, see Table I, with $\dot{V} = 0.71\,\mathrm{l/s}$. Generally, the numerical values of $\overline{u}$ are in good agreement with the experimental results. However, $\overline{u}$ is markedly overpredicted for $x < 0.15\,\mathrm{m}$ in all cases. This is probably due to the boundary condition at the top mould surface: In the experiment, there is a free surface and the fluid can be accelerated vertically by surface waves. On the contrary,

in the numerical model, the top surface of the mould is assumed to be flat and the fluid in the surface is accelerated horizontally towards the SEN.

From the inspection of the calculated profiles, it follows (i) all profiles of $\overline{u}$ are close to each other. Only between $x = 0.13$ and 0.25 m, slight variations between $C1$ (□), $C2$ (△) and $C3$ (▽) are present, (ii) $C1$ (□) and $C2$ (△) are nearly identical, and (iii) the differences between $C3$ (▽) and F (○) are small.

Figure 7 shows numerical and experimental data of the mean vertical velocity $\overline{w}(x)$ along line $L2$. Here, experimental data stem from PIV measurements in the left half (denoted as EL) and in the right half (denoted as ER) of the mould. These profiles are deduced from 10 sets of 200-s time averages. Nevertheless, there is a marked difference between the profile in the left and in the right half. Yuan *et al.* [3] assume, that transient flow structures with periods longer than 200 s exist in the flow, which can lead to asymmetric velocity profiles.

Again, the numerical data sets of $\overline{w}$ are in reasonable agreement with the experimental findings. But there is also a noticeable difference: The URANS simulation predicts an upward flow with $\overline{w} \sim 0.05$ m/s between $x = 0$ and 0.1 m, whereas the PIV data reveal upward velocities of only 0.01 m/s. Again, it can be assumed, that this difference is due to the expected long-term fluctuations in the lower mould, as explained in Reference [3].

The comparison of the different numerical profiles reveals (i) the profiles of $\overline{w}$ are close to each other, too. Only for $x > 0.34$ m, a small difference between $C3$ (▽) and the other numerical profiles is found. (ii) The zero-crossing of $\overline{w}$ at $x = 0.17$ m is well resolved in all simulation runs, and (iii) the differences between $C3$ (▽) and F (○) are again very small.

Figure 8 gives the time record of the time-filtered velocity $\langle u \rangle_{P1}$ at point $P1$ in simulation $C1$. The oscillating behaviour of the flow is evident. The amplitudes of $\langle u \rangle_{P1}$ are roughly twice the mean value $\overline{u}_{P1} = -0.10$ m/s of u in $P1$. This is again in good agreement with the experimental observations of Yuan *et al.* [3], they report oscillation amplitudes between 0.01 and -0.24 m/s for the horizontal velocity.

Figure 9 compares the first 250 s of $\langle u \rangle_{P1}$ in $P1$ from the simulations with different time step widths and grids. Obviously, the influence of the time-step and the grid resolution

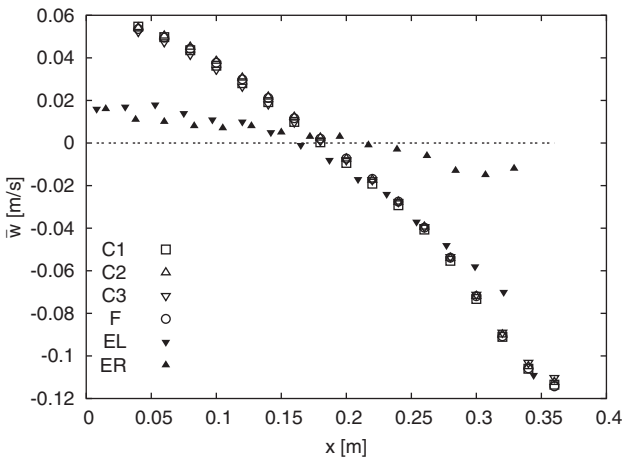

Figure 7. Mean vertical velocity $\overline{w}$ along $L2$, results are from numerical simulations ($C1$, $C2$, $C3$, F) and PIV measurements (EL, ER).

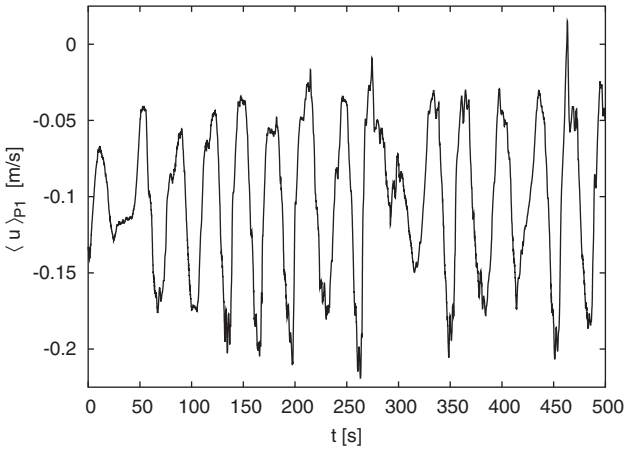

Figure 8. Time-filtered horizontal velocity $\langle u \rangle_{P1}$ at point $P1$, simulation $C1$.

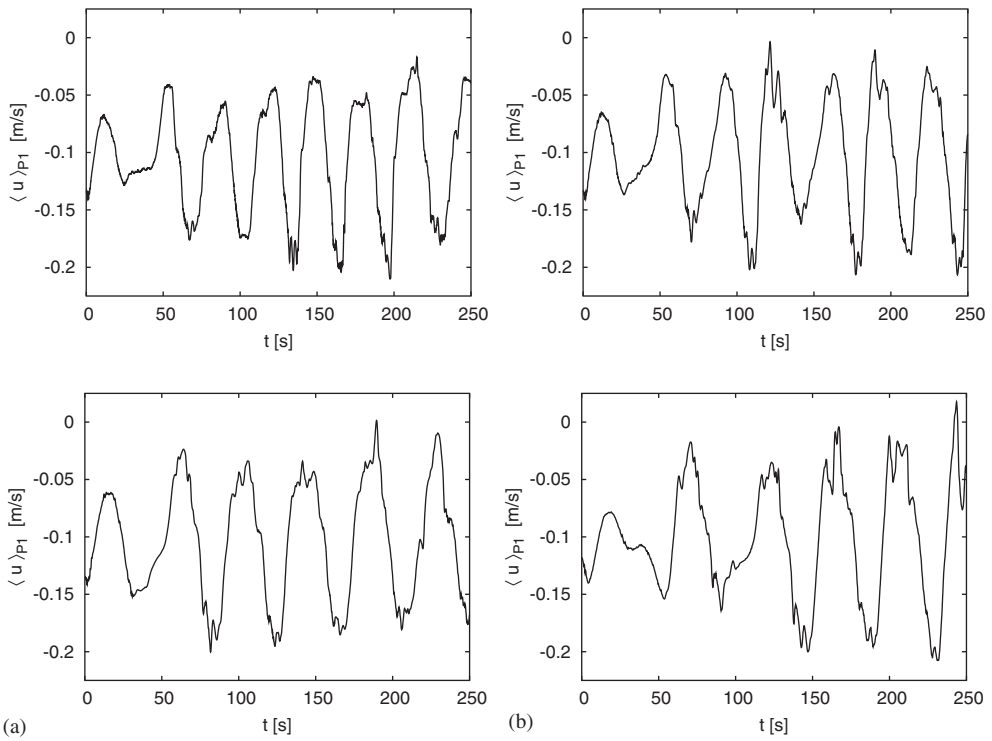

Figure 9. Time-filtered horizontal velocity $\langle u \rangle_{P1}$: (a) $C1$, $C3$; and (b) $C2$, F.

on the oscillation amplitudes is small, the oscillations extend between 0 and $-0.22\,\mathrm{m/s}$ in all cases.

The influence of the grid resolution on the oscillation periods is small, too. The periods in simulations F and $C3$ are nearly the same. On the contrary, the time step width Δt of the simulation can affect the results significantly. The oscillation periods in simulations $C1$ ($\Delta t_1 = 0.025\,\mathrm{s}$) and $C2$ ($\Delta t_2 = 0.05\,\mathrm{s}$) are close to each other, whereas the periods in simulations $C3$ and F ($\Delta t_3 = 0.1\,\mathrm{s}$) are markedly longer.

Fast Fourier transforms of the time records are given in Figure 10. All spectra exhibit a distinct peak frequency f_1. Only in the spectrum of simulation $C1$, a second peak is evident. The Fourier transforms confirm the previous interpretations of the time records: The peak frequencies of simulations $C1$, $f_{1,C1} = 0.032\,\mathrm{Hz}$, and $C2$, $f_{1,C2} = 0.029\,\mathrm{Hz}$, are markedly higher than the frequencies of simulations $C3$, $f_{1,C3} = 0.024\,\mathrm{Hz}$, and F, $f_{1,F} = 0.023\,\mathrm{Hz}$.

Figure 11 gives the time record of the time-filtered horizontal velocity $\langle u \rangle_{P2}$ at point $P2$ in simulation $C1$. Here, the signal corresponds to the superposition of at least two different oscillation frequencies.

The corresponding fast Fourier transform of simulation $C1$, Figure 12(a), confirms this interpretation. Two dominating frequency peaks $f_{2,C1,1} = 0.032\,\mathrm{Hz}$ and $f_{2,C1,2} = 0.06\,\mathrm{Hz}$ exist in the spectrum. The spectra of the other simulations $C2$, $C3$ and F show two peaks as well. However, corresponding to point $P1$, the peak frequencies of simulations $C1$ and case $C2$ are significantly higher than the peak frequencies of simulations $C3$ and F.

In Table II, the results of the simulations are compared with the experimental observations and the findings of the LES simulation by Yuan *et al.* [3]. They estimate an oscillation

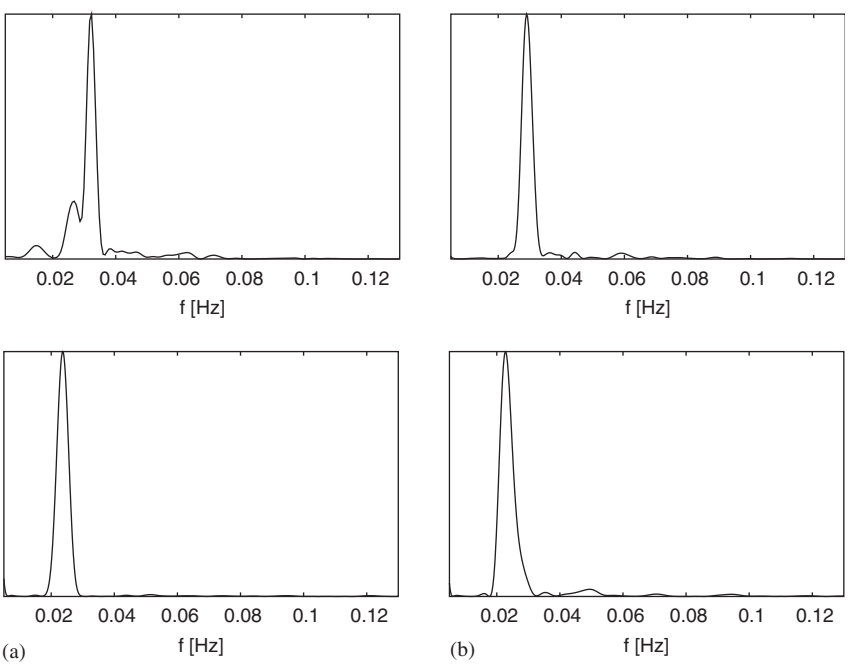

Figure 10. Fast Fourier transform of $\tilde{u}_{P1} = \langle u \rangle_{P1} - \overline{u}_{P1}$ in P1: (a) $C1$, $C3$; and (b) $C2$, F.

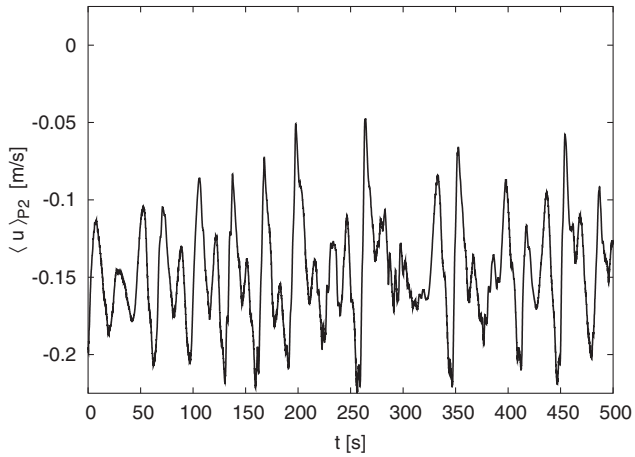

Figure 11. Time-filtered horizontal velocity $\langle u \rangle_{P2}$ at point $P2$, simulation $C1$.

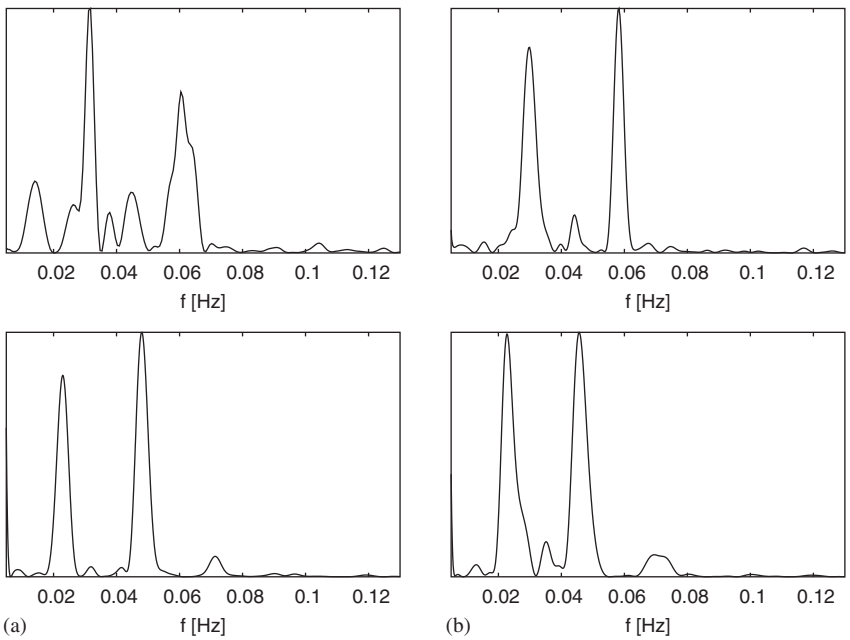

Figure 12. Fast Fourier transform of $\tilde{u}_{P2} = \langle u \rangle_{P2} - \overline{u}_{P2}$ in $P2$: (a) $C1$, $C3$; and (b) $C2$, F.

period $\tau_{\mathrm{PIV}} \simeq 45\,\mathrm{s}$ from the PIV measurements of u just beneath the upper mould surface as well. In the LES, u at the narrow face (at point $P2$) is found to oscillate with periods $\tau_{\mathrm{LES}} \sim 18\,\mathrm{s}$. Here, however, it has to be emphasized that the LES covers only 51 s of flow time. Hence, the LES cannot resolve the longer period adequately.

Table II. Oscillation periods in simulations and experiment.

		$C1$	$C2$	$C3$	F	LES [3]	Experiment [3]
$P1$	τ_1 [s]	31	34	43	45	—	45
$P2$	$\tau_{2,1}$ [s]	31	34	43	45	—	—
	$\tau_{2,2}$ [s]	17	17	21	22	18	—

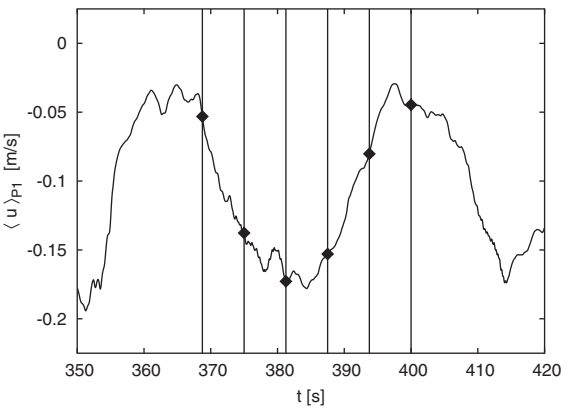

Figure 13. Oscillation period of $\langle u \rangle_{P1}$ at point $P1$, simulation $C1$.

Although the periods of the URANS simulations are in reasonable agreement with the data of Yuan *et al.* [3], significant differences are evident: The periods τ_1 in case $C1$ and $C2$ are about 30% shorter than in the experiment. It can be assumed, that these differences have to be addressed to the boundary condition at the top mould surface, too. As it has been discussed before, the prescribed flat top surface in the numerical model may cause a stronger horizontal acceleration of the fluid in the surface. This will in turn lead to a faster oscillation of $\langle u \rangle$ in $P1$ and $P2$.

Finally, two important results can be deduced from the comparison of the mean values and frequencies:

1. The influence of the grid size on the mean values, on the oscillation amplitudes, and on the oscillation frequencies is small.
2. The time step width impacts the oscillation amplitudes and the mean values of the velocity only slightly. On the contrary, the periods of the flow oscillations are noticeable shifted, when the time step width is not proper chosen.

3.3. *Features of the oscillating flow*

The structure of time-filtered velocity fields in the transient flows differ markedly from the steady state. Therefore, the behaviour of the velocity field is investigated for one oscillation period $369\,\mathrm{s} \leqslant t \leqslant 400\,\mathrm{s}$ in the simulation run $C1$, Figure 13. Features of the flow at $t = 369$ and 381 s are displayed in Figure 14. As all turbulent fluctuations are removed by the

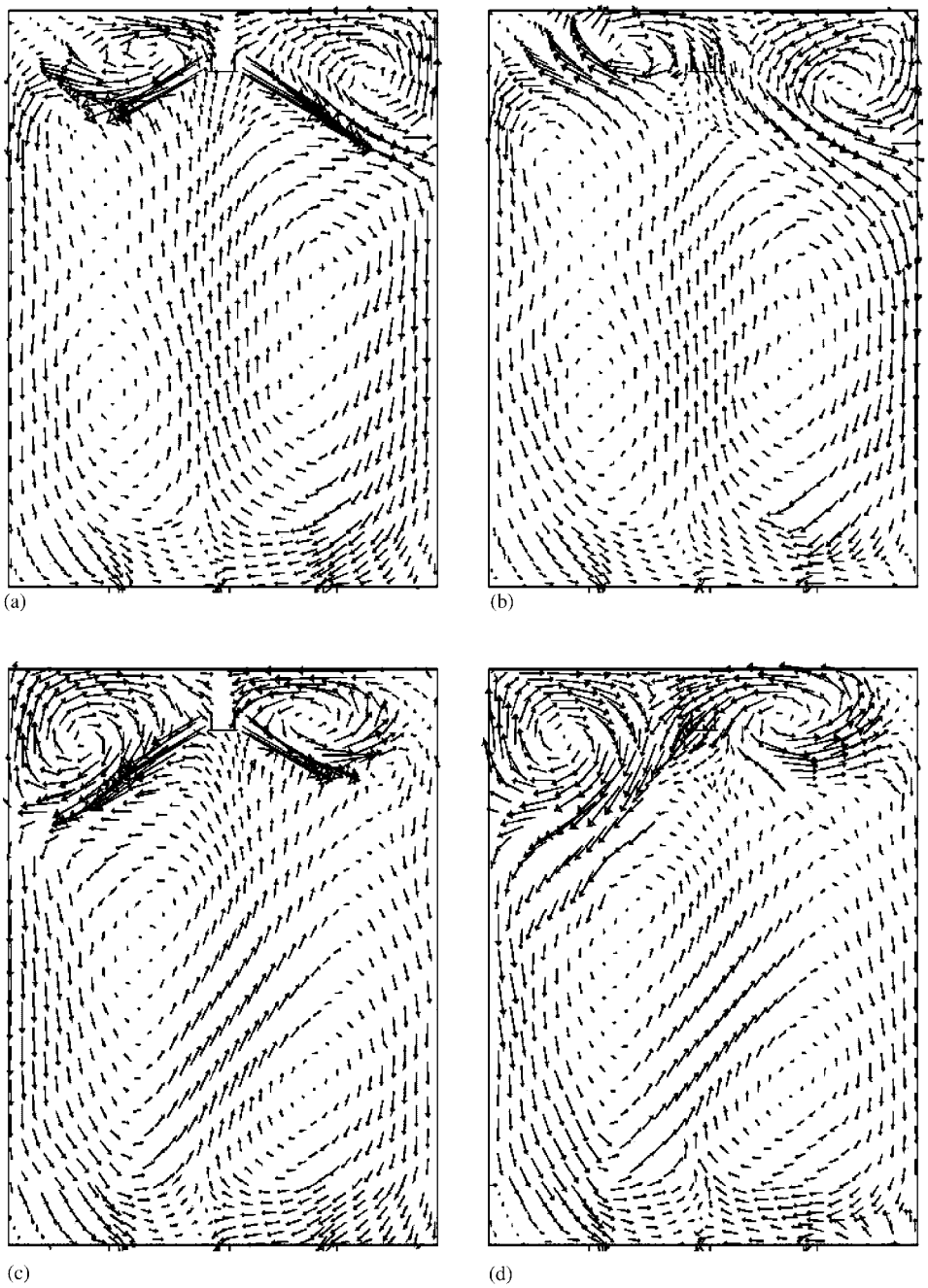

Figure 14. Time-filtered velocity vectors $\langle \mathbf{u} \rangle$ in the transient flow: (a) $t = 369\,\mathrm{s}$, $y = 0\,\mathrm{mm}$; (b) $t = 369\,\mathrm{s}$, $y = 33\,\mathrm{mm}$; (c) $t = 381\,\mathrm{s}$, $y = 0\,\mathrm{mm}$; and (d) $t = 381\,\mathrm{s}$, $y = 33\,\mathrm{mm}$.

time-filtering procedure, these results cannot be compared directly with instantaneous flow maps, e.g. from PIV measurements or LES simulations. At $t = 369$ and 381 s, $\langle u \rangle_{P1}$ is very near to its minimum and maximum value, respectively, Figure 13.

In the transient flow field, basic components, i.e. the jet streams, the upper and the lower rotating eddies, are still present. But they are not symmetrical. At $t = 369$ s, the upper right eddy is elongated, whereas the upper left eddy is shrinked with respect to the steady solution, Figures 14(a), (b) and 4. Later at $t = 381$ s, the alternations of the eddies are nearly inverted, Figure 14(c) and (d).

It is found, that the complete mould flow takes part in the oscillatory motion. This result is in good agreement with the qualitative observations of Gupta *et al.* [5]. They also report, that the complete mould flow pattern is mostly asymmetrical and oscillating.

3.4. Flow beneath the top-surface

The behaviour of the upper rotating eddies is of special interest for the casting process. Figure 15 shows these eddies for one oscillating period of the flow between $t = 369$ and 400 s in the simulation run $C1$. The right eddy is found to roll up to the SEN from $t = 369$ to 381 s. Subsequently, the right eddy swings back and reaches nearly its initial position at $t = 400$ s. The left eddy rolls up and swings back at a phase shift of a half period with respect to

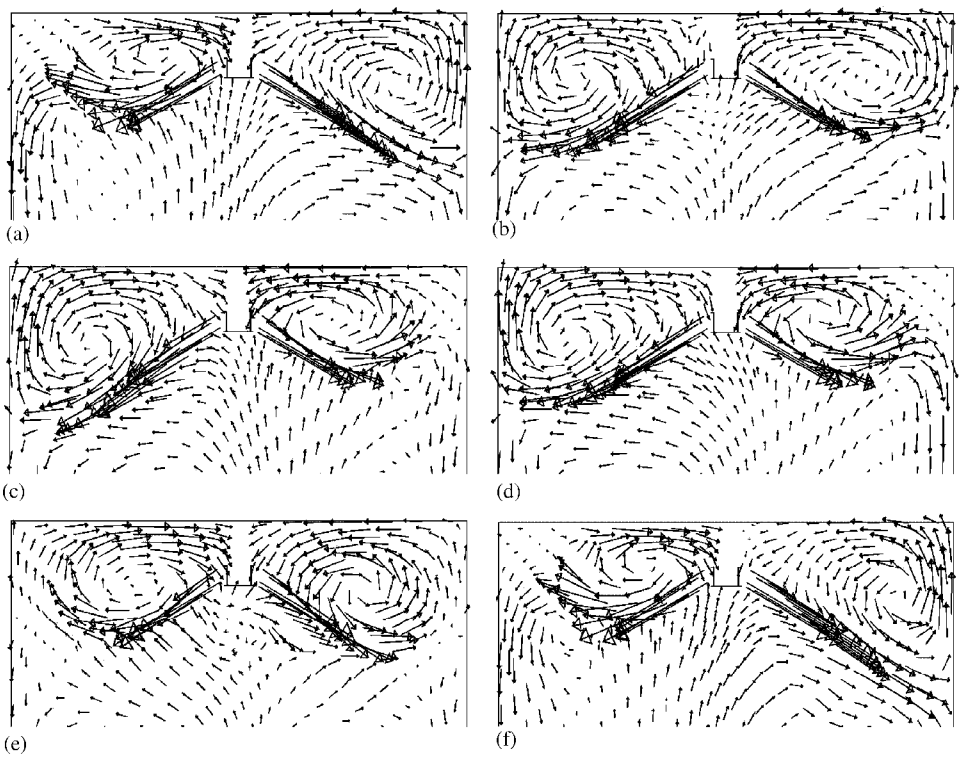

Figure 15. Velocity vectors $\langle \mathbf{u} \rangle$ in the vertical centreplane at $y = 0$ mm: (a) $t = 369$ s; (b) $t = 375$ s; (c) $t = 381$ s; (d) $t = 388$ s; (e) $t = 394$ s; and (f) $t = 400$ s.

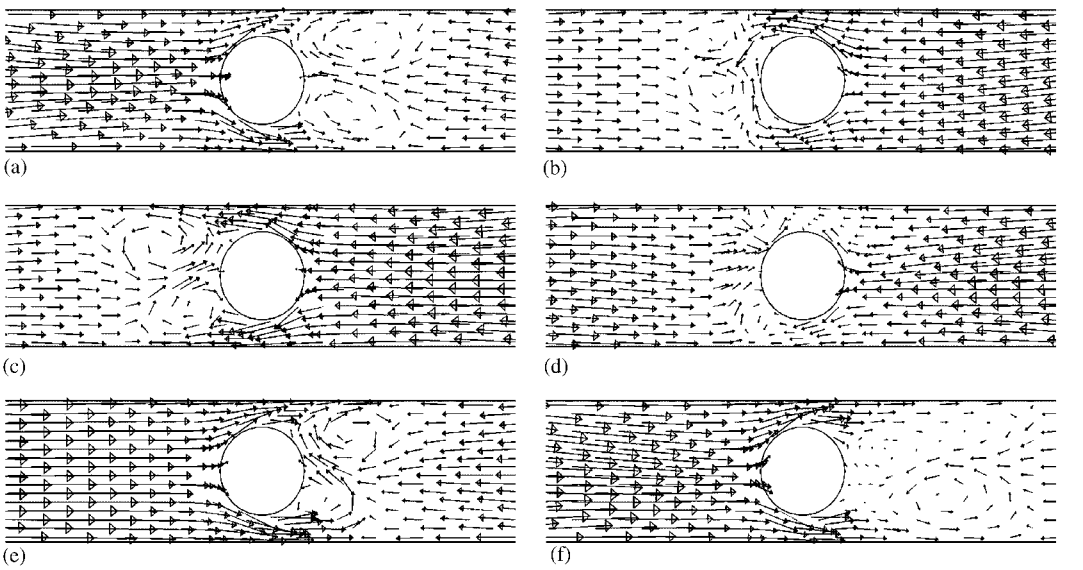

Figure 16. Velocity vectors $\langle \mathbf{u} \rangle$ in a horizontal plane at $z = -0.01$ m beneath the top mould surface: (a) $t = 369$ s; (b) $t = 375$ s; (c) $t = 381$ s; (d) $t = 388$ s; (e) $t = 394$ s; and (f) $t = 400$ s.

the right eddy. When an eddy rolls up towards the SEN, the amplitude of the near-surface velocity increases. On the contrary, the amplitude of the near-surface velocity decreases, when the eddy swings back to its initial position.

The oscillations of the upper rotating eddies drive important secondary flows near the SEN. Vectors of the time-filtered velocity $\langle \mathbf{u} \rangle$ in a horizontal plane just beneath the top mould surface are given in Figure 16. At $t = 369$ s, the velocity from the left side of the SEN is much larger than the velocity from the right, Figure 16(a). An overall flow to the right can be identified. This flow drives a strong vortex shedding on the right side of the SEN.

Between $t = 375$ and 381 s, the flow pattern changes significantly. Due to the roll up of the right eddy, Figure 15(b), the velocity from the right side of the SEN begins to overwhelm the velocity from the left side, Figure 16(b). Now, the overall flow direction is to the left side and first vortex structures can be seen on the left of the SEN. Vortex shedding on the left side of the SEN has developed until $t = 381$ s, Figure 16(c).

Finally, the flow pattern returns back into its initial structure at $t = 400$ s with a strong vortex shedding on the right side of the SEN, Figure 16(f). Now, the right eddy has been returned nearly into its initial position and begins to roll up, Figure 15(f).

These vortex shedding phenomena are of major importance for the continuous casting process. Funnel-shaped vortices can develop at the top mould surface, if vorticity exceeds critical limits. This funnel-shaped vortex tubes can be easily identified in water model experiments.

4. SUMMARY AND OUTLOOK

A numerical model of an oscillating continuous casting mould flow is presented. It is based on the unsteady Reynolds averaged equations (URANS) in combination with a Reynolds

stress turbulence model. Non-equilibrium wall functions are employed in order to describe the near-wall region of the turbulent flows.

Results of the URANS simulations are compared with corresponding results of a water model experiment and a large-eddy simulation (LES), which have been conducted by other authors. Mean values, amplitudes and frequencies which are deduced from the URANS data are in agreement with corresponding experimental observations and data from the LES simulation. However, the computational efforts of the URANS simulations are much lower than the ones of a LES simulation.

The numerical model can be used in order to examine the effects of the long-term flow oscillations on the performance of the continuous casting process of steel. An upgrade of the numerical model with respect to wavy free-surface flows should be made. This would permit the investigation of surface wave generation, which are frequently suspected to promote slag entrainment into the melt. In the present approach, the numerical model presumes, that the free mould surface remains flat. This simplification may be responsible slight deviations between numerical results and experimental data.

A complete description of the mould flow dynamics should also incorporate the flow in the SEN. This would permit a more detailed prediction of the velocity in the SEN ports, which also tends to an oscillating behaviour.

ACKNOWLEDGEMENTS

I would like to thank Prof. Dr F. Obermeier for very useful discussions. I also wish to thank the anonymous referees for their suggestions to improve the manuscript.

REFERENCES

1. Thomas BG. The importance of computational models for further improvements of the continuous casting process. In *Voest Alpine Conference on Continuous Casting*. Voest Alpine AG: Linz, 2000.
2. Thomas BG, Zhang L. Mathematical modeling of fluid flow in continuous casting. *ISIJ* 2001; **41**:1181–1193.
3. Yuan Q, Sivaramakrishnan S, Vanka SP, Thomas BG. Computational and experimental study of turbulent flow in a 0.4-scale water model of a continuous steel caster. *Metallurgical and Materials Transactions B* 2004; **35B**:967–982.
4. Huang X, Thomas BG. Modeling of transient flow phenomena in continuous casting of steel. *Canadian Metallurgical Quarterly* 1998; **37**:197–212.
5. Gupta D, Chakraborty S, Lahiri AK. Asymmetry and oscillation of the fluid flow pattern in a continuous casting mould: a water model study. *ISIJ International* 1997; **37**:654–658.
6. Ramos-Banderas A, Sanchez-Perez R, Morales RD, Palafox-Ramos J, Demedices-Garcia L, Diaz-Cruz M. Mathematical simulation and physical modeling of unsteady fluid flows in a water model of a slab mould. *Metallurgical Transactions B* 2004; **35B**:449–460.
7. Launder BE, Spalding DB. The numerical computation of turbulent flows. *Computer Methods in Applied Mechanics and Engineering* 1974; **3**:269–289.
8. Leschziner MA. Statistical turbulence modelling. In *New Trends in Turbulence*, Lesieur M, Yaglom A, David F (eds). Springer: Berlin, 2000.
9. Iaccarino G, Ooi A, Durbin PA, Behnia M. Reynolds averaged simulation of unsteady separated flow. *International Journal of Heat and Fluid Flow* 2003; **24**:147–156.
10. Schwarze R, Obermeier F. Modelling of unsteady electromagnetically driven recirculating melt flows. *Modelling and Simulation in Materials Science and Engineering* 2004; **12**:985–993.
11. Mataoui A, Schiestel R, Salem A. Flow regimes of interaction of a turbulent plane jet into a rectangular cavity: experimental approach and numerical modelling. *Flow Turbulence and Combustion* 2001; **67**:267–304.
12. Catalano P, Wang M, Iaccarino G, Moin P. Numerical simulation of the flow around a circular cylinder at high Reynolds numbers. *International Journal of Heat and Fluid Flow* 2003; **24**:463–469.
13. Johansen ST, Wu J, Shyy W. Filter-based unsteady RANS computations. *International Journal of Heat and Fluid Flow* 2004; **25**:10–21.

14. Launder BE, Reece GJ, Rodi W. Progress in the development of a Reynolds-stress turbulence closure. *Journal of Fluid Mechanics* 1975; **68**:537–566.
15. Lien FS, Leschziner MA. Assessment of turbulent transport models including non-linear RNG eddy-viscosity formulation and second-moment closure. *Computers and Fluids* 1994; **23**:983–1004.
16. Gibson MM, Launder BE. Grounds effects on pressure fluctuations in the atmospheric boundary layer. *Journal of Fluid Mechanics* 1978; **86**:491–511.
17. Kim SE, Choudhury D. A near-wall treatment using wall functions sensitized to pressure gradients. In *Separated and Complex Flows*, Otugen MV (ed.). ASME: New York, 1995.
18. Leonard BP. A stable and accurate convective modelling procedure based on quadratic upstream interpolation. *Computer Methods in Applied Mechanics and Engineering* 1979; **19**:59–98.
19. Rhie CM, Chow WL. Numerical study of the turbulent flow past an airfoil with trailing edge separation. *AIAA Journal* 1983; **21**:1525–1532.
20. Patankar SV, Spalding DB. A calculation procedure for heat, mass and momentum transfer in three-dimensional parabolic flow. *International Journal of Heat and Mass Transfer* 1972; **15**:1787–1806.
21. Casey M, Wintergerste T (eds). *Quality and Trust in Industrial CFD—Best Practice Guidelines*. ERCOFTAC, 2000.
22. Ferziger JH, Peric M. *Computational Methods for Fluid Dynamics* (3rd edn). Springer: Berlin, 2002; 333.

